Extended-Phase-Shift Control of Isolated Bidirectional DC–DC Converter for Power Distribution in Microgrid

Biao Zhao, *Student Member, IEEE*, Qingguang Yu, *Member, IEEE*, and Weixin Sun

***Abstract*—This paper points out a phenomenon of power backflow in traditional phase-shift (TPS) control of isolated bidirectional full-bridge DC–DC converter (IBDC), and analyzes the effects which backflow power act on power circulating flow and current stress. On this basis, the paper proposes a novel extended-phase-shift (EPS) control of IBDC for power distribution in microgrid. Compared with TPS control, EPS control not only expands regulating range of transmission power and enhances regulating flexibility, but also reduces current stress and improves the system efficiency. The operation principle of EPS control and the operation modes of IBDC are analyzed in the paper. By establishing mathematical models of transmission power, backflow power, and current stress, the paper comparatively analyzes control performances of TPS and EPS control. At last, experimental results verify the excellent performance of EPS control and correctness of the theoretical analysis.**

***Index Terms*—Bidirectional DC/DC converter, current stress., microgrid, phase-shift control, power distribution, power flow.**

I. Introduction

MICROGRIDS are becoming a reality in a scenario in which interconnected loads, distributed energy resources, and distributed storage systems can be conjugated and integrated into grid. The need for more flexible electricity systems, energy savings, and environmental impact are driving the development of microgrids [1]–[5].

Generally, microgrids can operate in grid-connected mode and islanded mode [6], [7]. In the grid-connected mode, the microgrid is connected to a utility grid, operates in parallel with the utility, and exchanges power with the utility through the point of common coupling. However, microgrid disconnects the utility and transfers into the islanded operation when a fault occurs in the upstream power grid. And in the islanded mode, microgrid can work as an autonomous grid to generate electricity using distributed energy resources. So it is important to balance demand and supply coming both from the utility and distributed energy resources.

Moreover, due to not only environmental aspects but also social, economical, and political interests, many types of renewable energy, such as photovoltaic (PV) and wind energy, have been widely utilized as distributed energy resources in microgrid [5]. But the variable nature of these renewable energy systems relies on natural phenomenon, such as sunshine or wind [8], [9]. Consequently, it is difficult to predict the power that can be obtained through these prime sources, and the peaks of power demand do not coincide necessarily with the generation peaks. Hence, storage energy systems are required if we want to supply the local loads in an uninterruptible power supply (UPS) fashion [5], [10].

In order to realize power distribution between energy generation systems and storage systems in micro grids, various bidirectional DC–DC converters (BDCs) have been proposed as an everlasting key component to interface between a high-voltage bus, where an energy generation system such as a fuel cell stack or a photovoltaic array is installed, and a low-voltage bus, where usually an energy storage system such as a battery or a super capacitor is implemented, as shown in Fig. 1 [11]. Generally, BDC is divided into nonisolated type [12], [13] and isolated type [11], [14]–[23], and galvanic isolation for BDC is required for flexibility of system reconfiguration and meeting safety standards [14], [17]. State-of-the-art isolated bidirectional DC–DC converter (IBDC) is based on the single-phase and H-bridge topology with a high-frequency isolation transformer. Fig. 2 depicts a typical configuration of IBDC. Compared to traditional DC–DC converter circuits, this converter has many advantages, such as electrical isolation, high reliability, easy to realize soft-switching control, and bidirectional energy flow [14]–[16], [20].

Generally, there are mainly two kinds of control methods for such topology: traditional pulsewidth modulation (PWM) control [17]–[19] and phase-shift control. In traditional PWM control, the cross-connected switch pairs in H-bridge (H_1), such as (S_1, S_4) and (S_2, S_3), are switched in turn to transform the high-voltage V_1 from DC to AC, the switches (Q_1–Q_4) in H-bridge (H_2) are turned OFF and the current conducts only through the diodes (M_1–M_4) to transform the voltage from AC to DC, so the power is transferred from V_1 side to V_2 side. In the reverse power flow, the states of S_1–S_4 and Q_1–Q_4 are exchanged. This control method is simple and easy to implement, but it has poor dynamic performance. And the AC output voltage can only be lower than DC input voltage in H-bridge inverter, so its regulating range of voltage is limited.

Manuscript received August 10, 2011; revised October 5, 2011 and November 13, 2011; accepted December 8, 2011. Date of current version June 20, 2012. This work was supported by the National Natural Science Foundation of China under Grant 51077076. Recommended for publication by Associate Editor T.-J. (Peter) Liang.

B. Zhao and Q. Yu are with the Department of Electrical Engineering, Tsinghua University, Beijing 100084, China (e-mail: zhaobiao112904829@126.com; yuqingguang@163.com).

W. Sun is with the China Power Engineering Consulting Group Corporation, North China Power Engineering Co. Ltd., Beijing 100084, China (e-mail: sunwx1023@163.com).

Color versions of one or more of the figures in this paper are available online at http://ieeexplore.ieee.org.

Digital Object Identifier 10.1109/TPEL.2011.2180928

0885-8993/$31.00 © 2012 IEEE

Authorized licensed use limited to: Electricity Generating Authority of Thailand. Downloaded on December 01,2021 at 07:50:17 UTC from IEEE Xplore. Restrictions apply.

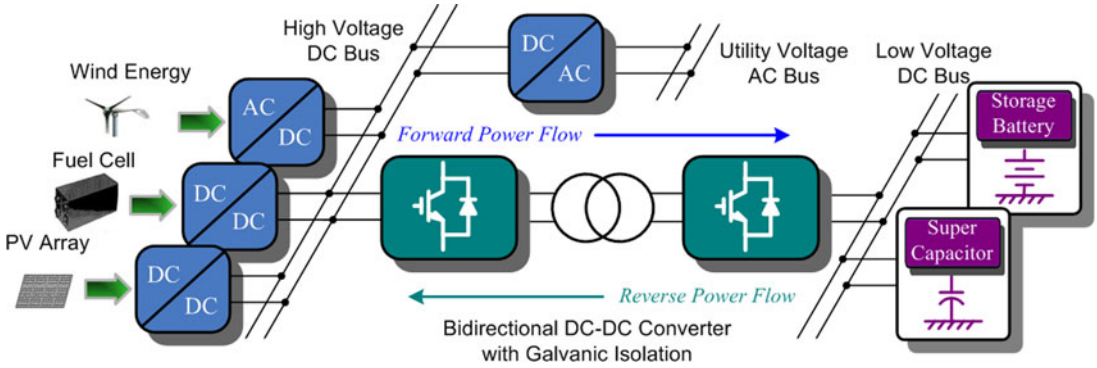


Fig. 1. Typical application of BDC for power distribution in microgrid [11].

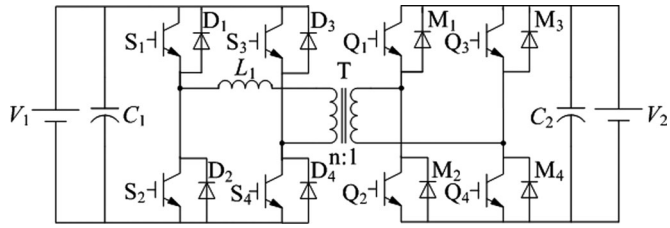


Fig. 2. Typical configuration of IBDC.

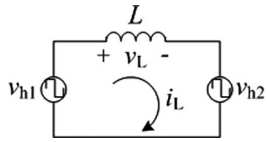


Fig. 3. Equivalent circuit of phase-shift control.

In TPS control [14]–[16], [20], the cross-connected switch pairs in both H-bridges (H_1 and H_2) are switched in turn to generate phase-shifted transition square waves to the transformer's primary and secondary sides. And the corresponding phase shift changes the voltage across the transformer's leakage inductor to manipulate the power flow direction and magnitude. This control method is attracting more and more attention due to its advantages such as small inertia, high dynamic performance, easy to realize soft-switching control, and so on. But in this method, the control of the power flow is dependent on transformer's leakage inductor that result in great circulating power and current stress when the value of V_1/nV_2 deviate far from 1, where n is turns' ratio of the transformer. And then, the loss in power devices and magnetic components is increased and the efficiency of converter is reduced. In order to improve the performance of the IBDC, various control methods were explored [21]–[25]. In some of these studies [21], [22], the duty ratio of the driving signals of each semiconductor device is variable, and should be calculated online, that increases the complexity of the control. Some studies are focused on how to extend the soft-switching range [23] or eliminate reactive power [24], the detailed analysis of steady characteristics is not conducted. In [25], a novel phase-shift dual-half-bridge converter with an adaptive inductor was proposed. It utilizes an adaptive inductor as the commutation inductor to adapt to the change of the output power, which results in strict requirements of the coiling method of inductor and the complexity of the control. And it is mainly improvement of hardware design; the control method of the proposed converter is still TPS control.

In view of the study situation mentioned above, this paper points out a phenomenon of power backflow in traditional phase-shift control, and analyzes the effects which backflow power act on power circulating flow and current stress. On this basis, the paper presents a novel extended-phase-shift control of IBDC for power distribution in microgrid. Different from the control methods mentioned above, this method adds another degree of freedom to the converter by adjusting the time sequence between the driving signals of diagonal semiconductor switches, e.g., (S_1, S_4) in Fig. 2. It not only has smaller power circulating flow and current stress, but also expands regulating range of transmission power and enhances regulating flexibility.

II. Phenomenon of Power Backflow in Traditional Phase-Shift Control

In Fig. 2, we replace the transformer with T-type equivalent circuit, and considering that the magnetizing inductance of the transformer is much greater than its leakage inductance, the magnetizing inductance can be considered as an open circuit. Therefore, the converter in phase-shift control can be represented by a simplified scheme comprised of two square waves voltage sources linked by an inductance L, as shown in Fig. 3.

In Fig. 3, L is the sum of the transformer leakage inductance and that of the auxiliary inductor L_1, $v_{\rm h1}$ and $v_{\rm h2}$ are the equivalent AC output voltages of H_1 and H_2 in V_1 side, respectively, v_L and i_L are the voltage and current of inductor L, respectively. The power-flow direction and magnitude can simply be controlled by adjusting the phase shift between $v_{\rm h1}$ and $v_{\rm h2}$. Here we take the forward power flow (from V_1 to V_2) as an example to analyze the main operation principle of TPS control.

The main waveforms of IBDC in TPS control are shown in Fig. 4, where $p_{\rm in}$ is the transient waveform of transmission power, $T_{\rm hs}$ is a half switching period, and D is the phase-shift ratio between the primary and secondary voltages of the isolation transformer, where $0 \le D \le 1$. And we assume $V_1 \ge nV_2$ in Fig. 4, the other condition $V_1 < nV_2$ can be analyzed similarly. Because $v_{\rm h1}$ and $v_{\rm h2}$ are both square wave AC voltages and their

Authorized licensed use limited to: Electricity Generating Authority of Thailand. Downloaded on December 01,2021 at 07:50:17 UTC from IEEE Xplore. Restrictions apply.

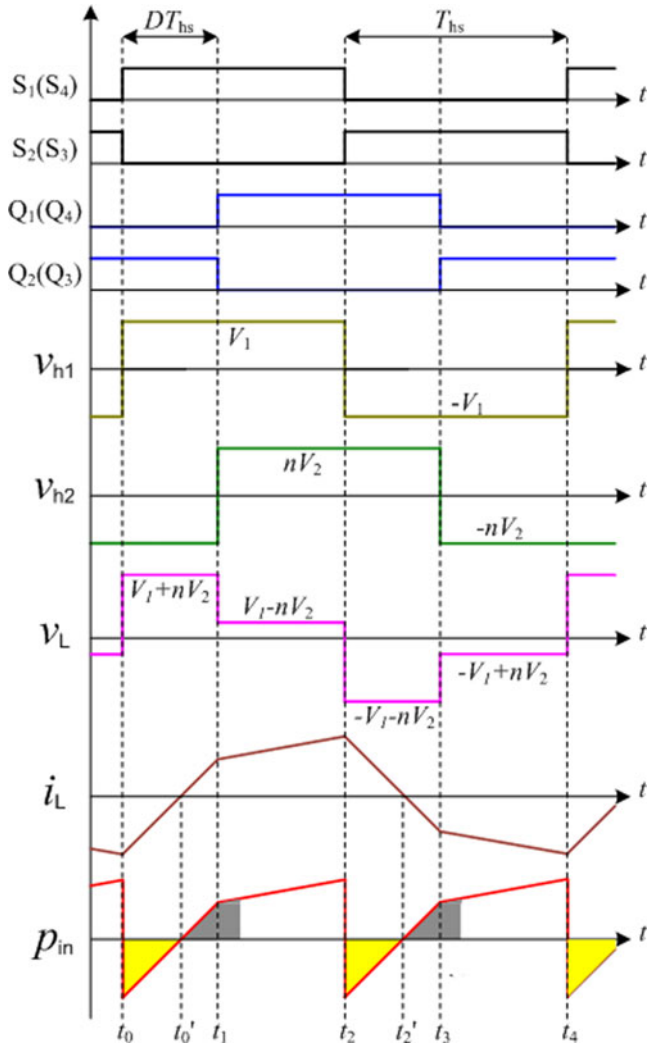


Fig. 4. Waveforms of IBDC in TPS control.

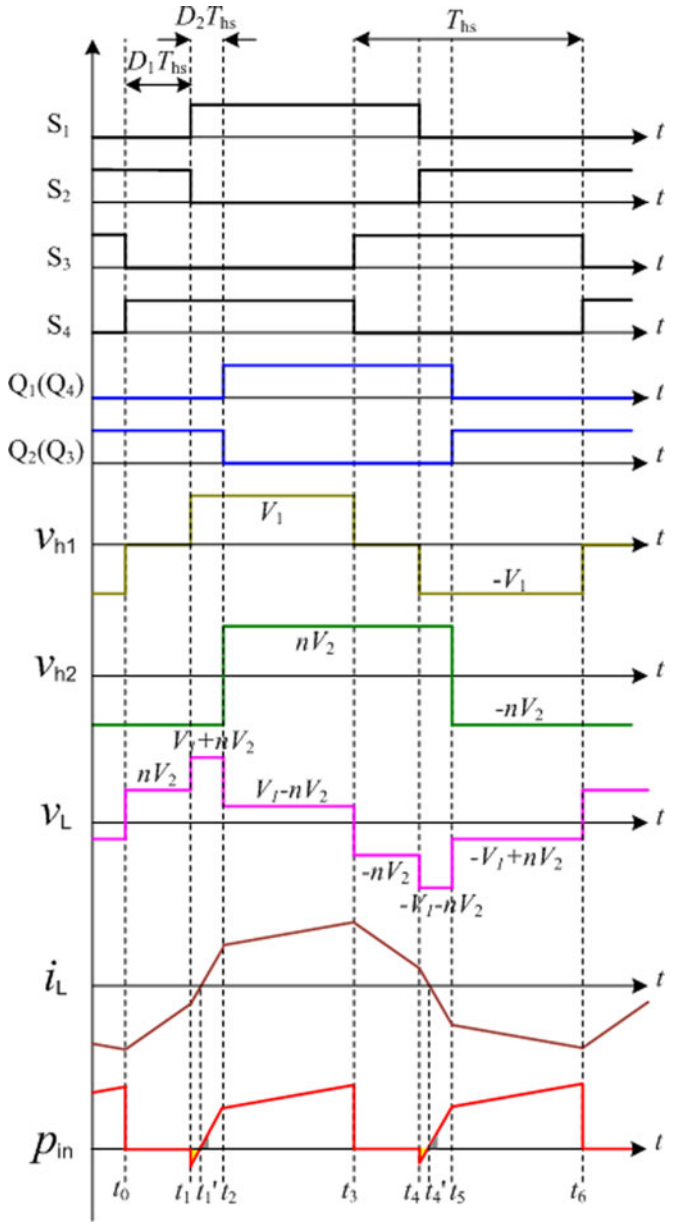


Fig. 5. Waveforms of IBDC in EPS control.

interaction is through the inductor L, so the phase of the primary current is not always the same as the primary voltage. As can be seen from Fig. 4, i_L is of the opposite phase from $v_{\rm h1}$ for an interval of $t = t_0 \sim t_0'$ and $t = t_2 \sim t_2'$, that is a portion of the power delivered to the V_2 side in one switching period, while the other portion is sent back to the primary voltage source V_1. We defined it as backflow power, which is the dark-shaded area in Fig. 4. For a given transmission power, with the increase of the backflow power, the forward power also increases to compensate the loss caused by backflow power. Then the circulating power and current stress are increased, which result in great loss in power devices and magnetic components and low efficiency of converter [16], [19]–[23]. In Section IV, we will establish a mathematical model to analyze it.

III. Operation Principle of Extended-Phase-Shift Control

A. Extended-Phase-Shift Control

In order to significantly decrease the backflow power of the converter, $v_{\rm h1}$ should not be confined to square waveforms with 50% duty ratio. For example, if S_1 and S_4 do not have the same driving signal but have a phase-shift ratio of D_1, as shown in Fig. 5, the transformer primary voltage will emerge as a three-level instead of the traditional two-level. Then the behaviors of i_L will also be changed: the backflow-appearance time ($t = t_0 \sim t_0'$ and $t = t_2 \sim t_2'$) in Fig. 4 are divided into two intervals ($t = t_0 \sim t_1$, $t = t_1 \sim t_1'$ and $t = t_3 \sim t_4$, $t = t_4 \sim t_4'$) in Fig. 5, respectively. And the transformer primary voltage $v_{\rm h1} = 0$, i.e., backflow power is 0, when $t = t_0 \sim t_1$ and $t = t_3 \sim t_4$. So the backflow power is decreased for a given transmission power. In the reverse power flow, we just need to exchange the operating states of the H-bridges H_1 and H_2.

In Fig. 5, D_1 is the phase-shift ratio between the driving signals of S_1 and S_4 or S_2 and S_3 in H-bridge H_1, we defined its inner phase-shift ratio, where $0 \le D_1 \le 1$. D_2 is the phase-shift

Authorized licensed use limited to: Electricity Generating Authority of Thailand. Downloaded on December 01,2021 at 07:50:17 UTC from IEEE Xplore. Restrictions apply.

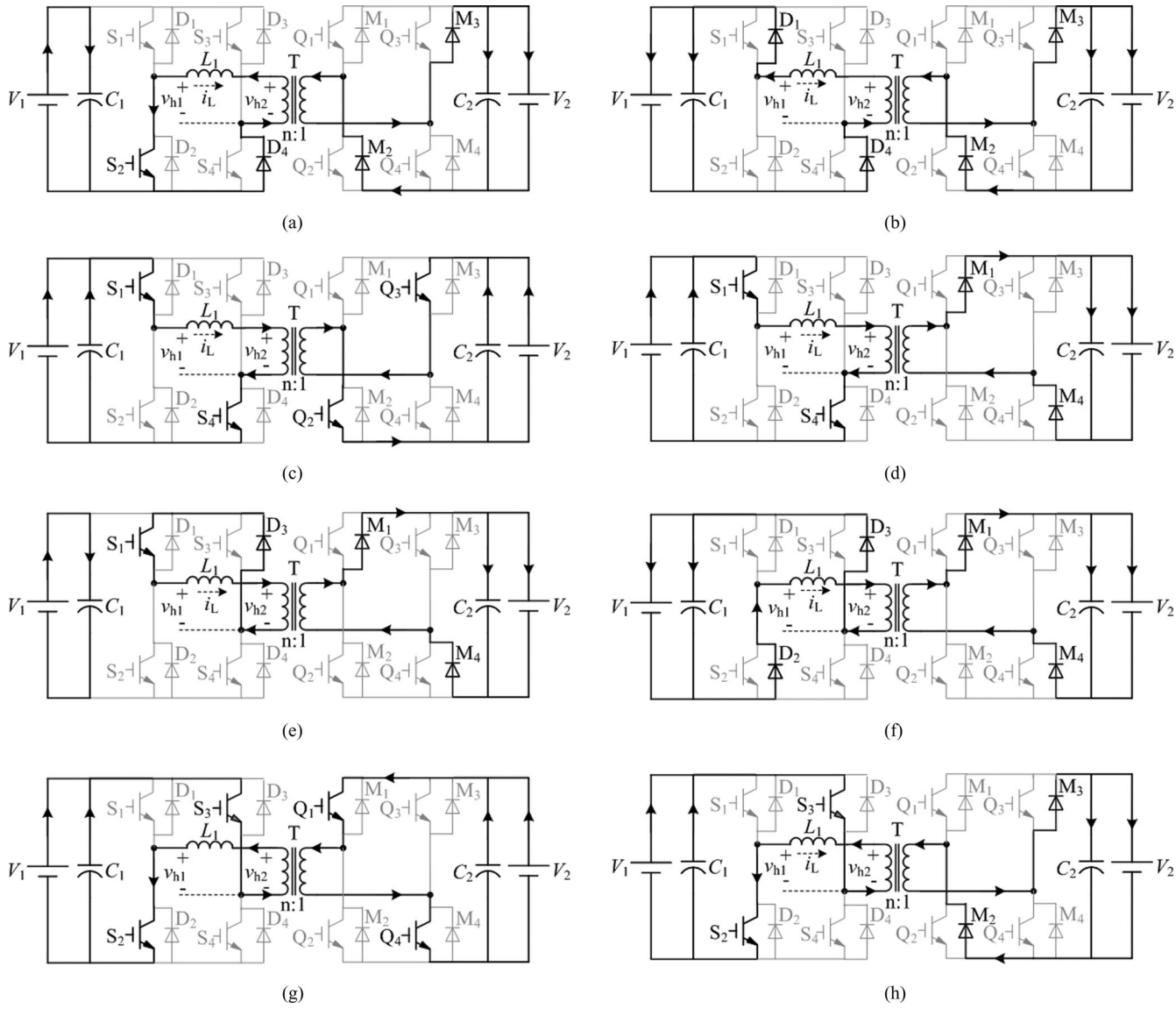


Fig. 6. Operation modes of IBDC in EPS control. (a) Mode 1. (b) Mode 2. (c) Mode 3. (d) Mode 4. (e) Mode 5. (f) Mode 6. (g) Mode 7. (h) Mode 8.

ratio between the primary and secondary voltages of the isolation transformer, we defined its outer phase-shift ratio, where $0 \leq D_2 \leq 1$ and $0 \leq D_1 + D_2 \leq 1$. In fact, compared to the TPS control, there is not only the outer phase-shift ratio but also the inner phase-shift ratio in the proposed EPS control, which will decrease the current stress, expands regulating range of transmission power and enhances regulating flexibility.

B. Operation Modes of IBDC in Extended-Phase-Shift Control

To simplify the process of the analysis, we assume that the converter has reached steady operation states. From Fig. 5, the switching cycle can be divided into eight operation modes which are explained as follows:

1) Mode 1 (t_0–t_1)*:* Fig. 6(a) shows the equivalent circuit for the mode *1*. Just before t_0, S_2 and S_3 are conducting. The current i_L is in negative direction. At t_0, S_3 is turned OFF and S_4 is turned ON at zero current, and D_4 starts to conduct. On the secondary side, the current is carried from L to V_2 by M_2 and M_3. The voltage across L is clamped at nV_2, and the current i_L decreases linearly. This mode ends up when S_2 is turned OFF. During this mode, the current of L is

$$i_L(t) = i_L(t_0) + \frac{nV_2}{L}(t - t_0). \tag{1}$$

2) Mode 2 (t_1–t_1')*:* Fig. 6(b) shows the equivalent circuit for mode 2. If current i_L is still in negative direction at t_1 then at t_1, S_2 is turned OFF and S_1 is turned ON at zero current, i_L is carried from L to V_1 by D_1 and D_4. On the secondary side, the current is carried from L to V_2 by M_2 and M_3. The voltage across L is clamped at $V_1 + nV_2$, and i_L still decreases linearly. This mode ends up with i_L decreasing to zero. During this mode, i_L is

$$i_L(t) = i_L(t_1) + \frac{V_1 + nV_2}{L}(t - t_1). \tag{2}$$

Authorized licensed use limited to: Electricity Generating Authority of Thailand. Downloaded on December 01,2021 at 07:50:17 UTC from IEEE Xplore. Restrictions apply.

3) Mode 3 (t_1'–t_2)*:* Fig. 6(c) shows the equivalent circuit for the mode 3. At t_1', the polarity of i_L changes from negative to positive. And because the driving signals of S_1, S_4, Q_2, and Q_3 are already on, so S_1, S_4, Q_2, and Q_3 start to conduct. The voltage across L is clamped at $V_1 + nV_2$, and i_L increases linearly. This mode ends up when Q_2 and Q_3 are turned OFF. During this mode, i_L is the same with (2).

4) Mode 4 ($t_2 - t_3$)*:* Fig. 6(d) shows the equivalent circuit for the mode *4*. At t_2, Q_2 and Q_3 are turned off and Q_1 and Q_4 are turned on at zero current. M_1 and M_4 start to conduct. The voltage across L is clamped at V_1–nV_2, and i_L still increases linearly due to $V_1 \geq nV_2$. This mode ends up when S_4 is turned OFF. During this mode, i_L is

$$i_L(t) = i_L(t_2) + \frac{V_1 - nV_2}{L}(t - t_2). \tag{3}$$

5) Mode 5 ($t_3 - t_4$)*:* Fig. 6(e) shows the equivalent circuit for mode *5*. At t_3, S_4 is turned OFF and S_3 is turned ON at zero current, D_3 starts to conduct. On the secondary side, the current is carried from L to V_2 by M_1 and M_4. The voltage across L is clamped at $-nV_2$, and the current i_L decreases linearly. This mode ends up when S_1 is turned OFF. During this mode, the current of L is

$$i_L(t) = i_L(t_3) + \frac{-nV_2}{L}(t - t_3). \tag{4}$$

6) Mode 6 ($t_4 - t_4'$)*:* Fig. 6(f) shows the equivalent circuit for mode *6*. If current i_L is still in positive direction at t_4, then at t_4, S_2 is turned OFF and S_1 is turned ON at zero current, i_L is carried from L to V_1 by D_2 and D_3. On the secondary side, the current is carried from L to V_2 by M_1 and M_4. The voltage across L is clamped at $-V_1$–nV_2, and i_L still decreases linearly. This mode ends up with i_L decreasing to zero. During this mode, i_L is

$$i_L(t) = i_L(t_4) + \frac{-V_1 - nV_2}{L}(t - t_4). \tag{5}$$

7) Mode 7 (t_4'–t_5)*:* Fig. 6(g) shows the equivalent circuit for the mode *7*. At t_4', the polarity of i_L changes from positive to negative. And, because the driving signals of S_2, S_3, Q_1, and Q_4 are already ON, so S_2, S_3, Q_1, and Q_4 start to conduct. The voltage across L is clamped at $-V_1$–nV_2, and i_L increases linearly. This mode ends up when Q_1 and Q_4 are turned OFF. During this mode, i_L is the same with (5).

8) Mode 8 ($t_5 - t_6$)*:* Fig. 6(h) shows the equivalent circuit for the mode *8*. At t_5, Q_1 and Q_4 are turned OFF and Q_2 and Q_3 are turned ON at zero current. M_2 and M_3 start to conduct. The voltage across L is clamped at $-V_1$+nV_2, and i_L still increases linearly due to $V_1 \geq nV_2$. This mode ends up when S_3 is turned OFF. During this mode, i_L is

$$i_L(t) = i_L(t_5) + \frac{-V_1 + nV_2}{L}(t - t_5). \tag{6}$$

According to the above analysis, the transformer primary voltage $v_{h1} = 0$, and there is no backflow power in modes *1* and *5*. So the whole backflow power is decreased for a given transmission power. In fact, if i_L has dropped to zero before t_1 or t_4, then the backflow power will be eliminated, as shown in Fig. 7(a). In this case, modes *2* and *6* in Fig. 6 will be replaced by mode *2′* and *6′* in Fig. 7(b) and (c), respectively.

9) Mode 2′ (t_1'–t_1)*:* Fig. 7(b) shows the equivalent circuit for mode *2′*. At t_1', the polarity of i_L changes from negative to positive. And because the driving signals of S_2, S_4, Q_2, and Q_3 are already ON, so D_2, S_4, Q_2, and Q_3 start to conduct. The voltage across L is clamped at nV_2, and i_L still increases linearly. This mode ends up when S_2 is turned OFF. During this mode, i_L is the same with (1).

10) Mode 6′ (t_4'–t_4)*:* Fig. 7(c) shows the equivalent circuit for mode *6′*. At t_4', the polarity of i_L changes from positive to negative. And because the driving signals of S_1, S_3, Q_1, and Q_4 are already ON, so D_1, S_3, Q_1, and Q_4 start to conduct. The voltage across L is clamped at $-nV_2$, and i_L still increases linearly. This mode ends up when S_1 is turned OFF. During this mode, i_L is the same with (4).

IV. Analysis and Comparisons of TPS And EPS Control

A. Low-Frequency Average Model

According to the above analysis, assuming $t_0 = 0$, then we have $t_1 = D_1T_{\rm hs}$, $t_2 = D_2T_{\rm hs}$, $t_3 = T_{\rm hs}$, $t_4 = T_{\rm hs}$+$D_1T_{\rm hs}$, $t_5 = T_{\rm hs}$+$D_2T_{\rm hs,}$ and $t_6 = 2T_{\rm hs}$. The average current of the inductors over one switching period ($2T_{\rm hs}$) should be zero in steady state; thus from (1) to (6), we can derive

$$i_L(t_0) = -\frac{nV_2}{4f_sL}[k(1 - D_1) + (2D_1 + 2D_2 - 1)] \tag{7}$$

$$i_L(t_1) = -\frac{nV_2}{4f_sL}[k(1 - D_1) + (2D_2 - 1)] \tag{8}$$

$$i_L(t_2) = \frac{nV_2}{4f_sL}[k(2D_2 + D_1 - 1) + 1] \tag{9}$$

where $f_s = 1/(2T_{\rm hs})$ is switching frequency, $k = V_1/nV_2$ is the voltage conversion ratio, and we assume $k \geq 1$ in the paper, the other condition $k < 1$ can be analyzed similarity. When the power flows from V_1 to V_2, the current stress of converter under EPS control is

$$i'_{\max} = |i_L(t_0)| = \frac{nV_2}{4f_sL}[k(1 - D_1) + (2D_1 + 2D_2 - 1)]. \tag{10}$$

The transmission power is

$$P' = \frac{1}{T_{hs}}\int_0^{T_{hs}} v_{\rm h1}i_L(t)dt = \frac{nV_1V_2}{2f_sL}\left[D_2(1 - D_2) + \frac{1}{2}D_1(1 - D_1 - 2D_2)\right]. \tag{11}$$

Authorized licensed use limited to: Electricity Generating Authority of Thailand. Downloaded on December 01,2021 at 07:50:17 UTC from IEEE Xplore. Restrictions apply.

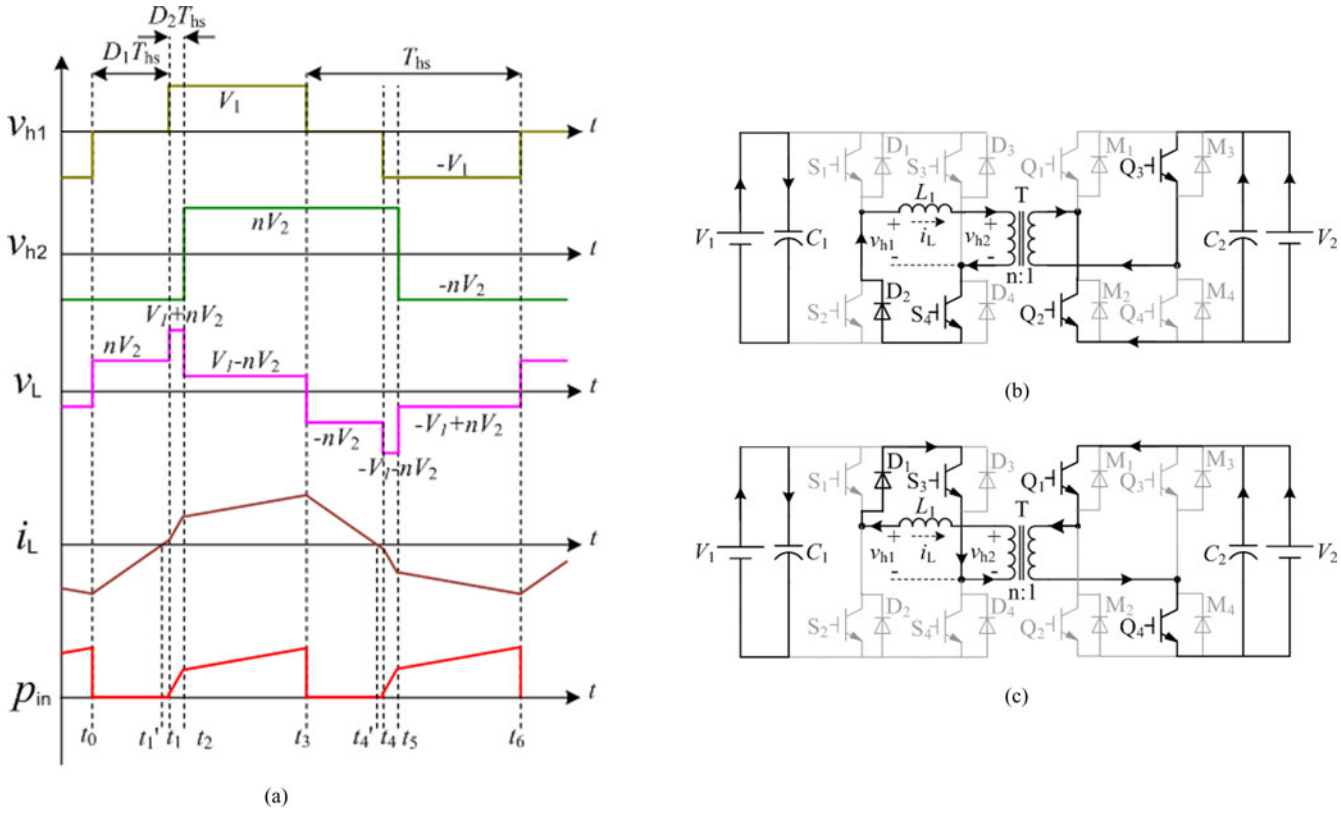


Fig. 7. (a) Waveforms of IBDC in EPS control when the backflow power is zero. (b) Mode 2′ of IBDC in EPS control when the backflow power is zero. (c) Mode 6′ of IBDC in EPS control when the backflow power is zero.

The backflow power is

$$P'_{bf} = \frac{1}{T_{hs}} \int_{t_1}^{t'_1} v_{\mathrm{h1}} \, |i_L(t)| dt = \frac{nV_1V_2[k(1-D_1)+(2D_2-1)]^2}{16f_sL(k+1)} \tag{12}$$

where $i_L(t_1) < 0$, from (8), we have

$$k > \frac{1-2D_2}{1-D_1}. \tag{13}$$

When $k \le (1–2D_2)/(1–D_1)$, the backflow power is zero. In (7)–(13), the constraints are $k \ge 1$, $0 \le D_1 \le 1$, $0 \le D_2 \le 1$, and $0 \le D_1+D_2 \le 1$. Similarly, from Fig. 4, the current stress of converter under TPS control is

$$i_{\max} = \frac{nV_2}{4f_sL}(2D-1+k). \tag{14}$$

The transmission power is

$$P = \frac{nV_1V_2}{2f_sL}D(1-D). \tag{15}$$

The backflow power is

$$P_{bf} = \frac{nV_1V_2[k+(2D-1)]^2}{16f_sL(k+1)}. \tag{16}$$

In (14)–(16), the constraints are $k \ge 1$ and $0 \le D \le 1$.

Theoretically, when the load is set as resistance R, from (11), we can derive

$$V_2 = \frac{nV_1R}{2f_sL}\left[D_2(1-D_2)+\frac{1}{2}D_1(1-D_1-2D_2)\right]. \tag{17}$$

With the variation of D_1 and D_2, we have

$$0 \le V_2 \le \frac{nV_1R}{8f_sL}. \tag{18}$$

Similarly, from (15), the output voltage range in the TPS control can be achieved. In fact, the output voltage range in the EPS control is the same as that in the TPS control. And its main benefit lies in that the power circulating flow and current stress are both reduced for a given output power; therefore, it leads to the improvement of the converter's overall efficiency. Theory and experiment analysis of the paper are centering on these special characteristics of EPS control as well.

B. Comparative Analysis of Transmission Power

For the convenience of analysis, the unified transmission power p' and p are defined as

$$\begin{cases} p' = \dfrac{P'}{P_N} = 4D_2(1-D_2)+2D_1(1-D_1-2D_2) \\ p = \dfrac{P}{P_N} = 4D(1-D) \end{cases} \tag{19}$$

Authorized licensed use limited to: Electricity Generating Authority of Thailand. Downloaded on December 01,2021 at 07:50:17 UTC from IEEE Xplore. Restrictions apply.

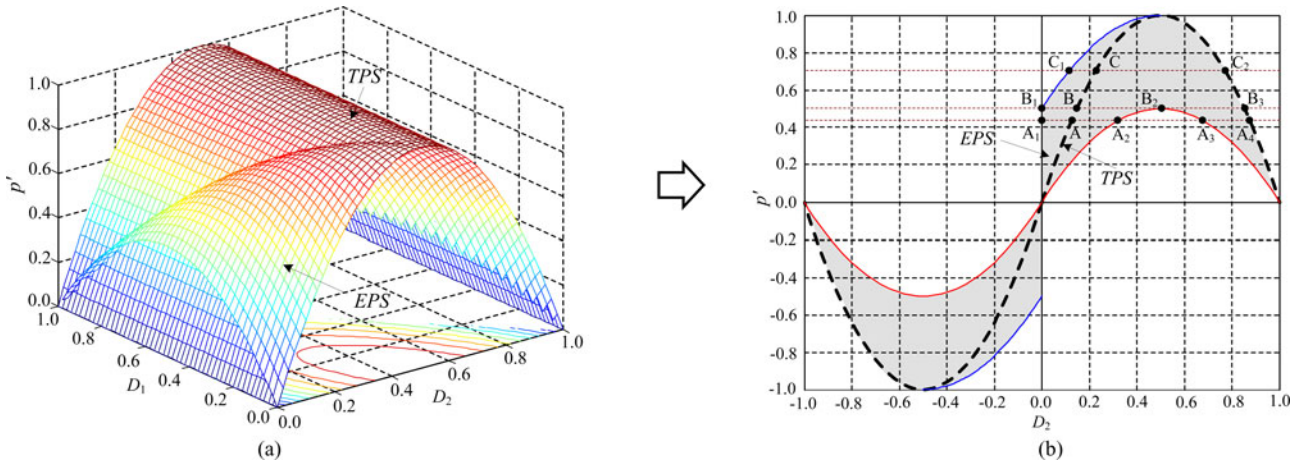


Fig. 8. Relation curves of the unified transmission power p' with D_1 and D_2. (a) 3-D curves. (b) 2-D curves.

where

$$P_N = \frac{nV_1V_2}{8f_sL}. \tag{20}$$

When taking that the outer phase-shift ratio (D_2) in EPS control is equal to the phase-shift ratio (D) in TPS control, the 3-D curves of the unified transmission power p' and p varied with D_1 and D_2 shown in Fig. 8(a). As can be seen from Fig. 8(a), with different D_1, p' will be different with p. And the EPS control can achieve larger transmission power than the TPS does when $0 \le D_2 < 0.5$. In fact, from (19), we can derive

$$p'_{\max} = 1 - \frac{(1-2D_2)^2}{2} \tag{21}$$

where $0 \le D_2 < 0.5$ and $D_1 = (1\text{-}2D_2)/2$.

$$p'_{\max} = 4D_2(1-D_2) \tag{22}$$

where $0.5 \le D_2 < 1$ and $D_1 = 0$.

$$p'_{\min} = 2D_2(1-D_2) \tag{23}$$

where $D_1 = 1\text{-}D_2$.

From (21) to (23), Fig. 8(a) can be converted to a 2-D picture, as shown in Fig. 8(b). The dashed line is the regulating curve of transmission power in TPS control, and the dark-shaded area is the regulating area of transmission power in EPS control. From Fig. 8(b), due to the addition of D_1, the regulating range of transmission power is changed from the single curve to the 2-D area. With the same outer phase-shift ratio ($D_2 = D$), the EPS control offers wider power transmission range than the TPS control does, and the maximum value is determined by (21) and (22) while the minimum value is determined by (23). Due to the addition of D_1, the regulating flexibility of transmission power is also enhanced.

Considering that the basic prerequisite for comparative analysis of backflow power and current stress is that the transmission power of TPS and EPS control are the same. In the following analysis, we take operating points A/A_4, B/B_3, and C/C_2 as characteristic points of TPS control in different operating areas, where $A(D = 1/8)$, $A_4(D = 7/8)$, $B(D = (2 - 2^1/2)/4)$, $B_3(D = (2+2^1/2)/4)$, $C(D = 1/4)$, and $C_2(D = 3/4)$, then the characteristic points of EPS control are $A_1/A_2/A_3$, B_1/B_2, and C_1.

C. Comparative Analysis of Backflow Power

Considering the relationship between the backflow power and the transmission power, the unified backflow power M_bf and M'_{bf} are defined as

$$M'_{bf} = \frac{P'_{bf}}{P_N} = \frac{[k(1-D_1)+(2D_2-1)]^2}{2(k+1)} \tag{24}$$

$$M_{bf} = \frac{P_{bf}}{P_N} = \frac{[k+(2D-1)]^2}{2(k+1)}. \tag{25}$$

The basic prerequisite for comparative analysis of backflow power is that the transmission power of TPS and EPS control are the same. From (11) and (15), we have

$$4D(1-D) = 4D_2(1-D_2) + 2D_1(1-D_1-2D_2). \tag{26}$$

With the specified value of D_1 and D_2 in EPS control, the phase-shift ratio D in TPS control can be obtained

$$D = \begin{cases} D' = \dfrac{1-\sqrt{1-4D_2(1-D_2)-2D_1(1-D_1-2D_2)}}{2} \\ D'' = \dfrac{1+\sqrt{1-4D_2(1-D_2)-2D_1(1-D_1-2D_2)}}{2} \end{cases}. \tag{27}$$

Using (24), (25), and (27), and assuming $k = 5$, the 3-D curve of the unified backflow power varied with D_1 and D_2 can be shown in Fig. 9. As can be seen from Fig. 9, the backflow power in TPS and EPS control are the same when $D_1 = 0$. And due to the addition of D_1, with the same transmission power, the backflow power in TPS control is larger than that in EPS control, and the condition of $D = D''$ generates larger backflow power than the condition of $D = D'$ does.

The contour lines in Fig. 8(b) show that there are infinite combinations of (D_1, D_2) in EPS control for the same transmission power in TPS control. Considering the different qualities of EPS control in different operating points, we will analyze the

Authorized licensed use limited to: Electricity Generating Authority of Thailand. Downloaded on December 01,2021 at 07:50:17 UTC from IEEE Xplore. Restrictions apply.

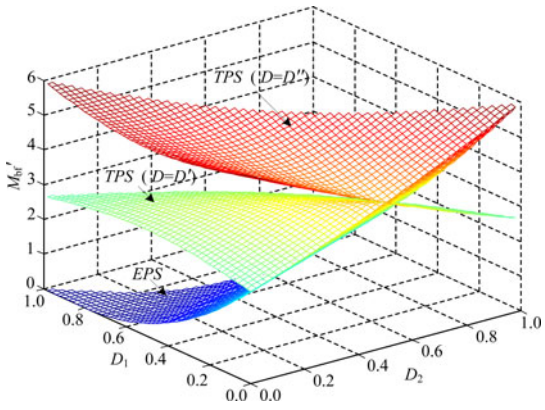


Fig. 9. 3-D curves of the unified backflow power $M'_{\rm bf}$ varied with D_1 and D_2.

optimal operating point of backflow power. From (26), we have

$$D_1 = \begin{cases} D_1' = \dfrac{1-2D_2-\sqrt{2(1-2D)^2-(1-2D_2)^2}}{2} \\ D_1'' = \dfrac{1-2D_2+\sqrt{2(1-2D)^2-(1-2D_2)^2}}{2} \end{cases}. \tag{28}$$

For $D_1'' \geq D_1'$, from (24), we have

$$M'_{bf}(D_1') \geq M'_{bf}(D_1''). \tag{29}$$

Substituting $D_1 = D_1''$ into (24), the function of $M'_{\rm bf}$ and D_2 can be obtained

$$M'_{bf\,\min}(D_2) = \frac{[k(1-\sqrt{2(1-2D)^2-(1-2D_2)^2})+2(k+2)D_2-2]^2}{8(k+1)} \tag{30}$$

where $|1\text{–}2D_2| \leq 2^1/2\ |1\text{–}2D|$ and $0 \leq D_2 \leq 1$. Solving (30) with constrained optimization methods, we can derive

1) when $0 \leq D < (2\text{–}2^1/2)/4$

$$M'_{bf\,\min}(D_2) = M'_{bf\,\min}(0) = \frac{[k-2-k\sqrt{2(1-2D)^2-1}]^2}{8(k+1)} \tag{31}$$

where

$$\begin{cases} D_1 = \dfrac{1+\sqrt{2(1-2D)^2-1}}{2} \\ D_2 = 0 \end{cases} \tag{32}$$

2) when $(2\text{–}2^1/2)/4 \leq D < 1/2$

$$M'_{bf\,\min}(D_2) = M'_{bf\,\min}\left(\frac{1-\sqrt{2}(1-2D)}{2}\right) = \frac{[(\sqrt{2}-1)k-2+2(k+2)D]^2}{4(k+1)} \tag{33}$$

where

$$\begin{cases} D_1 = \dfrac{\sqrt{2}(1-2D)}{2} \\ D_2 = \dfrac{1-\sqrt{2}(1-2D)}{2}. \end{cases} \tag{34}$$

In Fig. 8(b), we take operating points A, B, C, $A_1/A_2/A_3$, B_1/B_2, and C_1 as characteristic points of TPS and EPS control in different operating areas, from (19) to (21), and (26), we have: $A_1(D_2 = 0, D_1 = (4+2^1/2)/8)$, $A_1'(D_2 = 0, D_1 = (4\text{–}2^1/2)/8)$, $A_2(D_2 = (4\text{–}2^1/2)/8, D_1 = (4+2^1/2)/8)$, $A_3(D_2 = (4+2^1/2)/8, D_1 = (4\text{–}2^1/2)/8)$, $B_1(D_2 = 0, D_1 = 1/2)$, $B_2(D_2 = 1/2, D_1 = 1/2)$, and $C_1(D_2 = (2\text{–}2^1/2)/4, D_1 = 2^1/2/4)$. Fig. 10 shows the curves of the unified backflow power varied with voltage conversion ratio k in TPS and EPS control for the same transmission power.

D. Comparative Analysis of Current Stress

For the convenience of analysis, the unified current stress G' and G are defined as

$$G' = \frac{i'_{\max}}{I_N} = 2[k(1-D_1)+(2D_1+2D_2-1)] \tag{35}$$

$$G = \frac{i_{\max}}{I_N} = 2(2D-1+k) \tag{36}$$

where

$$I_N = \frac{P_N}{V_1} = \frac{nV_2}{8f_sL}. \tag{37}$$

Using (27), (35), and (36), and assuming $k = 5$, the 3-D curve of the unified current stress varied with D_1 and D_2 as shown in Fig. 11. As can be seen from Fig. 11, the current stress in TPS and EPS control are the same when $D_1 = 0$. And due to the addition of D_1 with the same transmission power, the current stress in TPS control is larger than that in EPS control, and the condition of $D = D''$ generates larger current stress than the condition of $D = D'$ does.

Likewise, the optimal operating point of current stress can be analyzed. For $D_1'' \geq D_1'$, from (35), we have

$$\begin{cases} G'(D_1') \leq G(D_1'') & k < 2 \\ G'(D_1'') \leq G(D_1') & k \geq 2. \end{cases} \tag{38}$$

That is,

$$G'_{\min}(D_2) = \begin{cases} (k-2)\sqrt{2(1-2D)^2-(1-2D_2)^2} \\ \qquad +2kD_2+k \quad k<2 \\ (2-k)\sqrt{2(1-2D)^2-(1-2D_2)^2} \\ \qquad +2kD_2+k \quad k\geq 2 \end{cases} \tag{39}$$

where $|1\text{–}2D_2| \leq 2^1/2\ |1\text{–}2D|$ and $0 \leq D_2 \leq 1$. Solving (39) with constrained optimization methods, we can derive

1) when $0 \leq D < (2\text{–}2^1/2)/4$

$$G'_{\min}(D_2) = \begin{cases} (k-2)\sqrt{2(1-2D)^2-1}+k & k<2 \\ (2-k)\sqrt{2(1-2D)^2-1}+k & k\geq 2 \end{cases} \tag{40}$$

Authorized licensed use limited to: Electricity Generating Authority of Thailand. Downloaded on December 01,2021 at 07:50:17 UTC from IEEE Xplore. Restrictions apply.

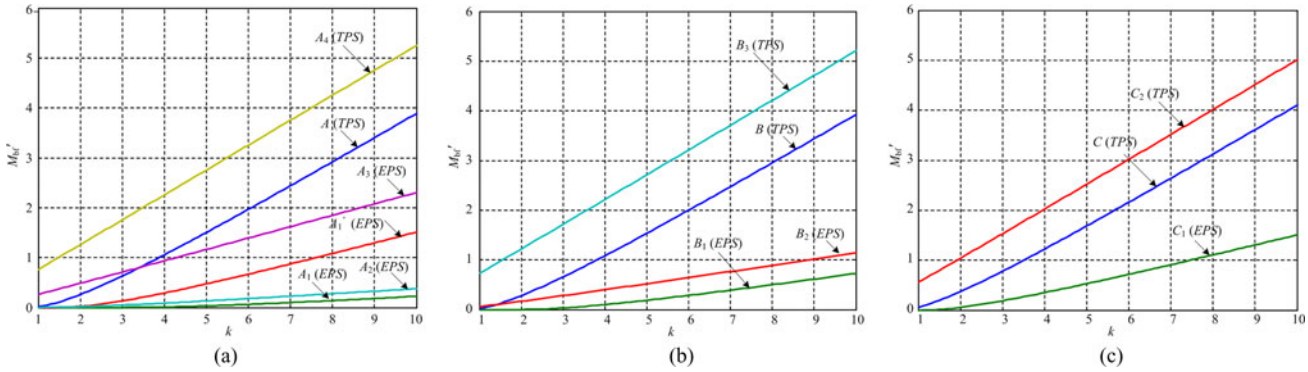


Fig. 10. Curves of the unified backflow power M'_{bf} varied with voltage conversion ratio k. (a) A and A_4 in TPS control and A_1, A'_1, A_2, and A_3 in EPS control. (b) B and B_3 in TPS control and B_1 and B_2 in EPS control. (c) C and C_2 in TPS control and C_1 in EPS control.

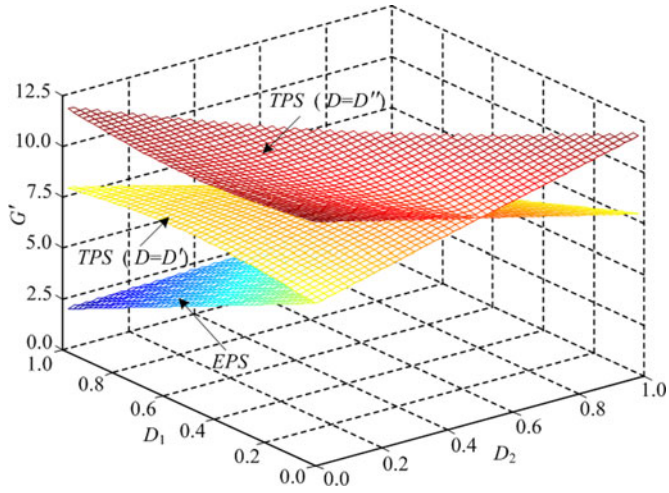


Fig. 11. 3-D curves of the unified current stress G' varied with D_1 and D_2.

where

$$\begin{cases} D_1 = \begin{cases} \dfrac{1-\sqrt{2(1-2D)^2-1}}{2} & k<2 \\ \dfrac{1+\sqrt{2(1-2D)^2-1}}{2} & k\geq 2 \end{cases} \\ D_2 = 0. \end{cases} \tag{41}$$

According to (32) and (41), when $k \geq 2$, the optimal operating points of backflow power and current stress are the same. From (36) and (40), we can derive

$$\begin{cases} G \leq G'_{\min} & k<k_0 \\ G'_{\min} \leq G & k\geq k_0 \end{cases} \tag{42}$$

$$k_0 = 2 - \frac{1+\sqrt{2(1-2D)^2-1}}{2(1-D)} \tag{43}$$

2) when $(2–2^1/2)/4 \leq D < 1/2$

$$G'_{\min}(D_2) = k(2\sqrt{2}D + 2 - \sqrt{2}) \tag{44}$$

where

$$\begin{cases} D_1 = \dfrac{\sqrt{2}(1-2D)}{2} \\ D_2 = \dfrac{1-\sqrt{2}(1-2D)}{2}. \end{cases} \tag{45}$$

From (36) and (44), we can derive

$$\begin{cases} G \leq G'_{\min} & k<k_0 \\ G'_{\min} \leq G & k\geq k_0 \end{cases} \tag{46}$$

where

$$k_0 = \sqrt{2}. \tag{47}$$

According to the above analysis, when $k \geq k_0$, the current stress in EPS control is less than that in TPS control. Likewise, we take operating points A, B, C, $A_1/A_2/A_3$, B_1/B_2, and C_1 as characteristic points of TPS and EPS control in different operating areas. Then the curves of the unified current stress varied with voltage conversion ratio k for the same transmission power shown in Fig. 12.

As can be seen from Fig. 12, in all operating areas, the current stress increases with the increase of voltage conversion ratio k. The EPS control can take different operating points to ensure that the current stress is less than the TPS control when $k \geq k_0$, and the minimum value is obtained at A_1, B_1, and C_1, which agrees well with the aforementioned theoretical analysis.

V. Experimental Results

In order to verify the aforementioned analysis, a laboratory prototype is constructed based on TMS320F2812 DSP. And the main parameters of converter are shown in Table I.

In order to verify the power regulating capacity of EPS control, the input voltage and the output load are specified as 220 V and 6 Ω, respectively. Fig. 13 shows the curves of the transmission power varied with D_1 and D_2. As can be seen from Fig. 13, in EPS control, the transmission power can be regulated both by D_1 and D_2, and due to the addition of D_1, the regulating range

Authorized licensed use limited to: Electricity Generating Authority of Thailand. Downloaded on December 01,2021 at 07:50:17 UTC from IEEE Xplore. Restrictions apply.

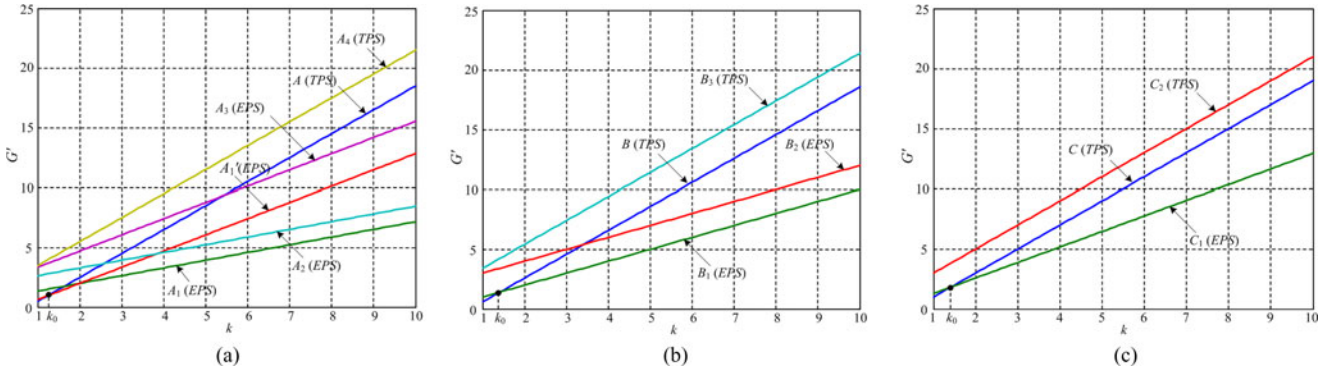


Fig. 12. Curves of the unified current stress G' varied with voltage conversion ratio k. (a) A and A_4 in TPS control and A_1, $A_1{}'$, A_2, and A_3 in EPS control. (b) B and B_3 in TPS control and B_1 and B_2 in EPS control. (c) C and C_2 in TPS control and C_1 in EPS control.

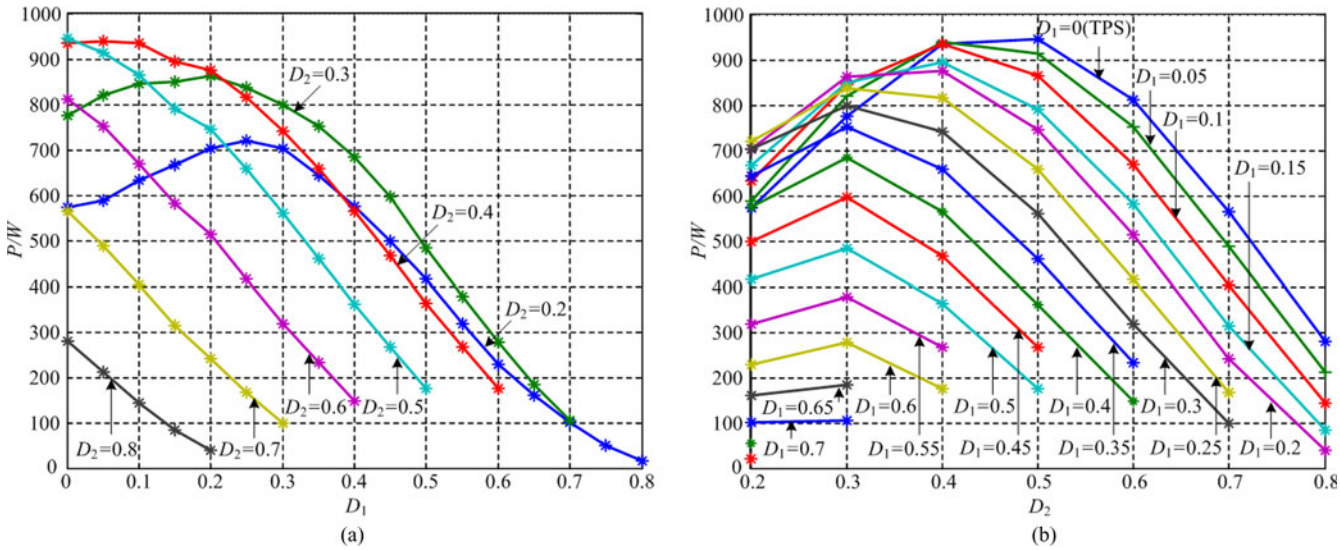


Fig. 13. Curves of the transmission power varied with D_1 and D_2. (a) Curves of the transmission power varied with D_1 when D_2 is specified. (b) Curves of the transmission power varied with D_2 when D_1 is specified.

TABLE I
MAIN PARAMETERS OF PROTOTYPE

Auxiliary inductor	L_1	0.2 mH
Input dc capacitor	C_1	2200 μH
Output dc capacitor	C_1	2200 μH
Transformer voltage ratio	n	2
Switching frequency	f	10 kHz
Input dc voltage	V_1	140 ~ 300 V
Output dc voltage	V_2	0 ~ 180 V
Output power	P_2	0 ~ 1160W
Output load	R_2	6/28Ω

of transmission power is changed from the single curve to the 2-D area. With the same outer phase-shift ratio ($D_2 = D < 0.5$), the EPS control ($D_1 \neq 0$) can offer wider power transmission range than the TPS control ($D_1 = 0$) does, that will enhance regulating flexibility. In addition, Fig. 13 shows that there are many different combinations of (D_1, D_2) in EPS control for the same transmission power in TPS control. And the maximum and minimum values of transmission power are obtained about at $D_1+D_2 = 0.5$ and $D_1+D_2 = 1$, respectively, which agrees well with the aforementioned theoretical analysis.

In order to verify the backflow power characterization of EPS control, the transmission power and output voltage are both in closed-loop control for 380 W and 48 V, respectively, the transient waveforms of transmission power with input voltage $V_1 = 220$ V is shown in Fig. 14(a), and the curves of backflow power varied with input voltage V_1 and inner phase-shift ratio D_1 is shown in Fig. 14(b). It can be seen from Fig. 14, the backflow power is bound up with input voltage V_1 and inner phase-shift ratio D_1, and it decreases with the increase of D_1 and increases with the increase of voltage conversion ratio $k = V_1/(nV_2)$. Under different experimental conditions, the EPS control always can generate less backflow power than the TPS control does, and the minimum point of current stress is the minimum point of

Authorized licensed use limited to: Electricity Generating Authority of Thailand. Downloaded on December 01,2021 at 07:50:17 UTC from IEEE Xplore. Restrictions apply.

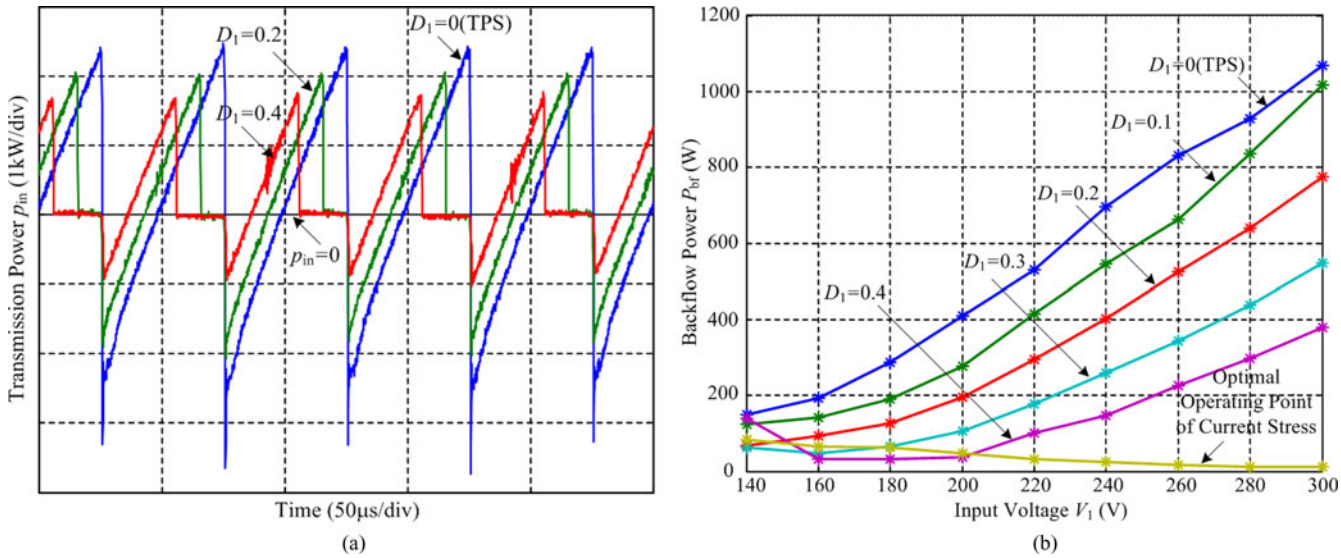


Fig. 14. (a) Transient waveforms of the transmission power when D_1 is specified. (b) Curves of the backflow power varied with V_1 when D_1 is specified.

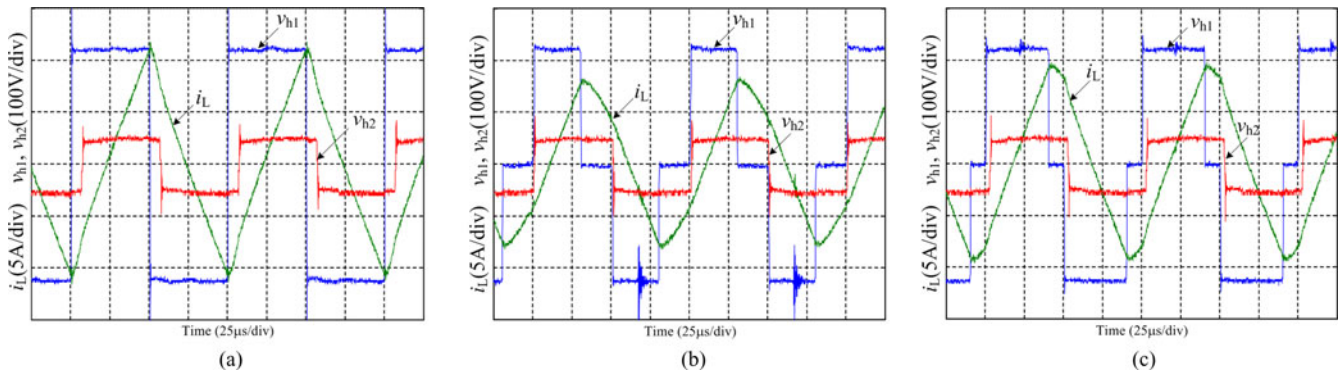


Fig. 15. Waveforms of v_{h1}, v_{h2}, and i_L in TPS and EPS control for the same transmission. (a) TPS control with $V_1 = 220$ V, $V_2 = 48$ V, and $P = 380$ W. (b) EPS control with $V_1 = 220$ V, $V_2 = 48$ V, $P' = 380$ W, and $D_1 = 0.2$. (c) EPS control with $V_1 = 220$ V, $V_2 = 48$ V, $P' = 380$ W, and $D_1 = 0.4$.

backflow power when $V_1 > 200$ (i.e., $k > 200/(2*48) \approx 2$), which agrees well with the aforementioned theoretical analysis.

Fig. 15 shows the experimental waveforms of v_{h1}, v_{h2}, and i_L in TPS and EPS control for the same transmission power, and Fig. 16 shows the curves of current stress varied with V_1 and D_1. It can be seen that current stress is also bound up with input voltage V_1 and inner phase-shift ratio D_1, and it decreases with the increase of D_1 and increases with the increase of voltage conversion ratio $k = V_1/(nV_2)$. Under different experimental conditions, the EPS control always can generate less current stress than the TPS control does. When the converter is operating in the optimal point, the stress current achieves the minimum value, which is consistent with the aforementioned theoretical analysis.

Under the same experimental conditions with Figs. 14(b) and 16, Fig. 17 shows the efficiency curves of the converter in both control methods. It can be easily found that the EPS control can achieve higher efficiency than the TPS control, especially in large voltage conversion ratio condition. And when the converter

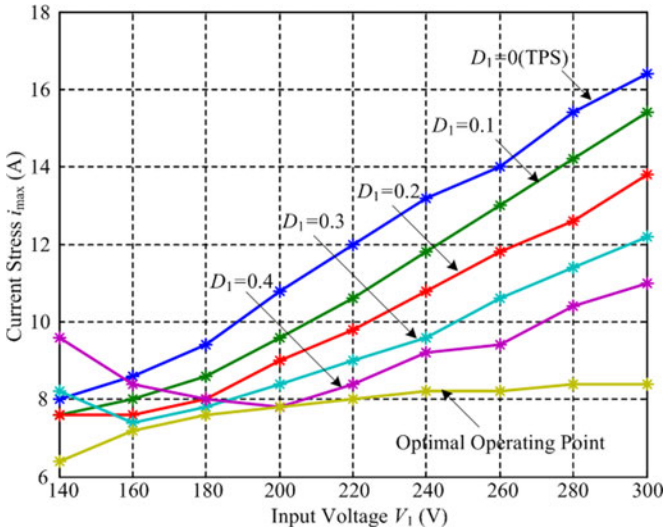


Fig. 16. Curves of the current stress varied with V_1 when D_1 is specified.

Authorized licensed use limited to: Electricity Generating Authority of Thailand. Downloaded on December 01,2021 at 07:50:17 UTC from IEEE Xplore. Restrictions apply.

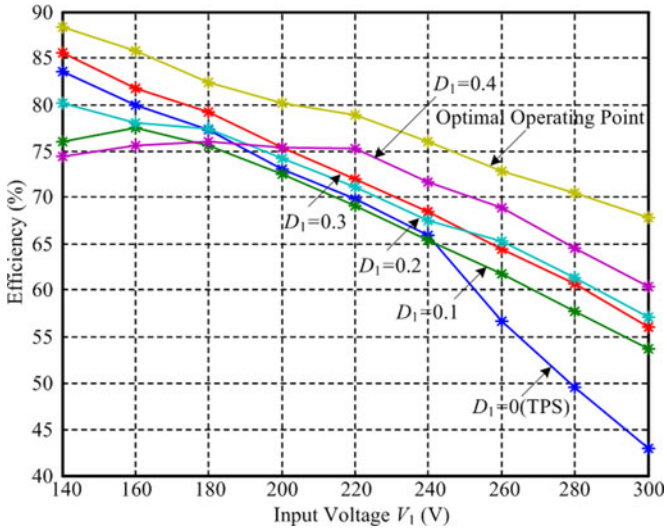


Fig. 17. Curves of the efficiency curves varied with V_1 when D_1 is specified.

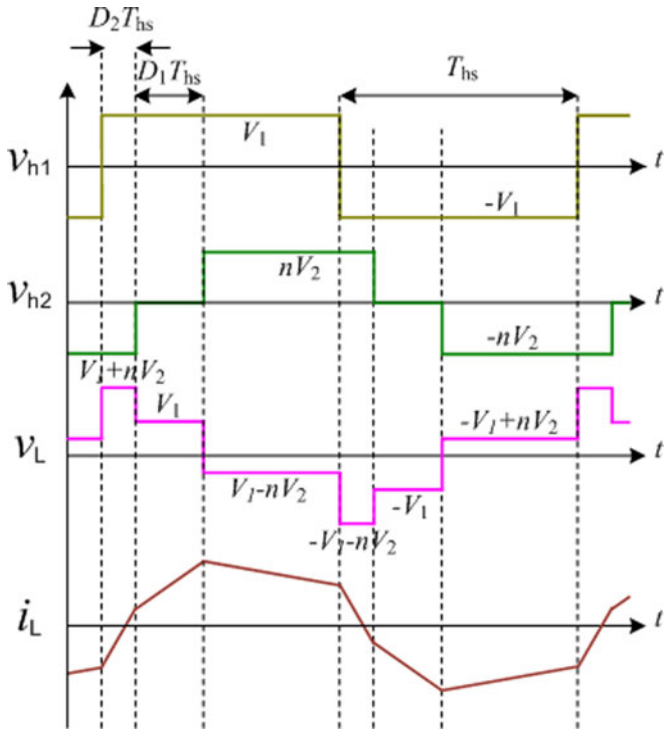


Fig. 18. Waveforms of IBDC in EPS control when $k < 1$.

is operating in the optimal point, the efficiency achieves the maximum value.

VI. Discussion

All of the above analysis is based on the qualification that $k \geq 1$. In fact, when $k < 1$ ($nV_2 > V_1$), we just need to exchange the operating modes of the left and the right H-bridges, as shown in Fig. 18.

Similar to the analysis in Sections I and IV, we can derive that the current stress of converter under EPS control is

$$i'_{\max} = \frac{V_1}{4f_sL}\left[\frac{1}{k}(1-D_1)+(2D_1+2D_2-1)\right]. \quad (48)$$

The transmission power is

$$P' = \frac{nV_1V_2}{2f_sL}\left[D_2(1-D_2)+\frac{1}{2}D_1(1-D_1-2D_2)\right]. \quad (49)$$

The backflow power is

$$P'_{bf} = \frac{nV_1V_2[(1/k)(1-D_1)+(2D_2-1)]^2}{16f_sL(1/k)+1)}. \quad (50)$$

In (48)–(50), the constraints are $k < 1, 0 \leq D_1 \leq 1, 0 \leq D_2 \leq 1$ and $0 \leq D_1+D_2 \leq 1$. Similarly, the current stress of converter under TPS control is

$$i_{\max} = \frac{V_1}{4f_sL}(2D-1+(1/k). \quad (51)$$

The transmission power is

$$P = \frac{nV_1V_2}{2f_sL}D(1-D). \quad (52)$$

The backflow power is

$$P_{bf} = \frac{nV_1V_2[(1/k)+(2D-1)]^2}{16f_sL(1/k)+1)}. \quad (53)$$

In (51)–(53), the constraints are $k < 1$ and $0 \leq D \leq 1$. Due to $1/k > 1$, comparing (48)–(53) with (9)–(12) and (14)–(16), we can come to the conclusion that the performance at $k < 1$ is coincident with that at $k > 1$.

The transmission power and output voltage are both in closed-loop control for 1160 W and 180 V, respectively. Fig. 19 shows the experimental waveforms of v_{h1}, v_{h2}, and i_L in TPS and EPS control for the same transmission power, and Fig. 20 shows the curves of current stress varied with V_1 and D_1. Different with Fig. 15, the input voltage in Fig. 19 is specified as 160 V, i.e., $k = 160/(2*180) = 0.44$. As can be seen from Figs. 19 and 20, the current stress also decreases with the increasing of D_1, but decreases with the increasing of $k = V_1/(nV_2)$. In fact, when $k < 1$ ($nV_2 > V_1$), the current stress changes into an increase with the increasing of voltage conversion ratio $1/k = nV_2/V_1$. Similarly, the EPS control always can generate less current stress than the TPS control does with the condition of $k < 1$.

Fig. 21 shows the efficiency curves of the converter in both control methods. It can be easily found that the EPS control can achieve higher efficiency than the TPS control, especially in large voltage conversion ratio condition. And when the converter is operating in the optimal point, the efficiency achieves the maximum value.

Authorized licensed use limited to: Electricity Generating Authority of Thailand. Downloaded on December 01,2021 at 07:50:17 UTC from IEEE Xplore. Restrictions apply.

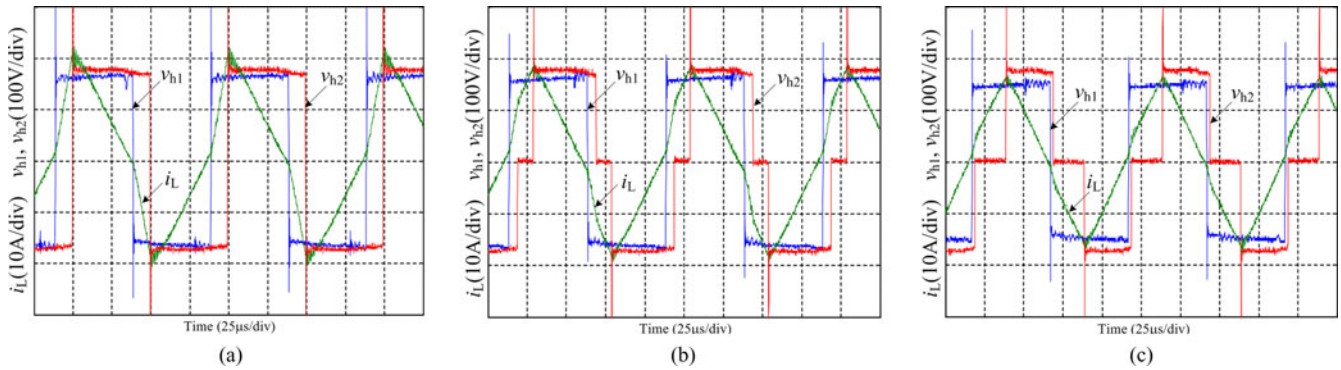


Fig. 19. Waveforms of v_{h1}, v_{h2}, and i_L in TPS and EPS control for the same transmission. (a) TPS control with $V_1 = 160$ V, $V_2 = 180$ V, and $P = 1160$ W. (b) EPS control with $V_1 = 160$ V, $V_2 = 180$ V, $P' = 1160$ W, and $D_1 = 0.2$. (c) EPS control with $V_1 = 160$ V, $V_2 = 180$ V, $P' = 1160$ W, and $D_1 = 0.4$.

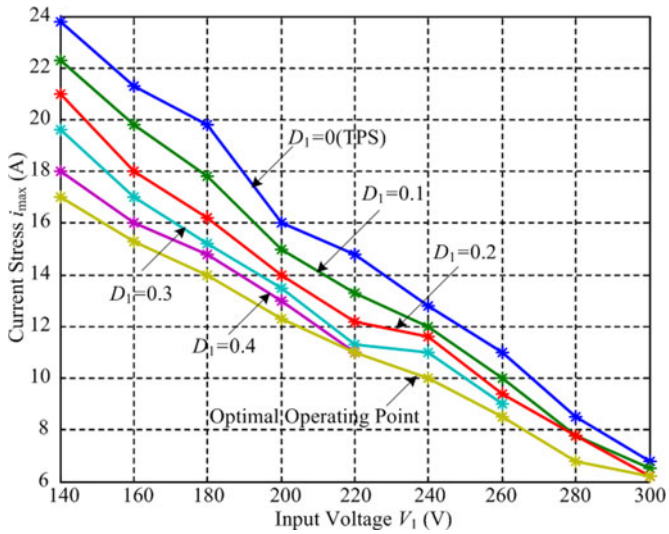


Fig. 20. Curves of the current stress varied with V_1 ($k < 1$) when D_1 is specified.

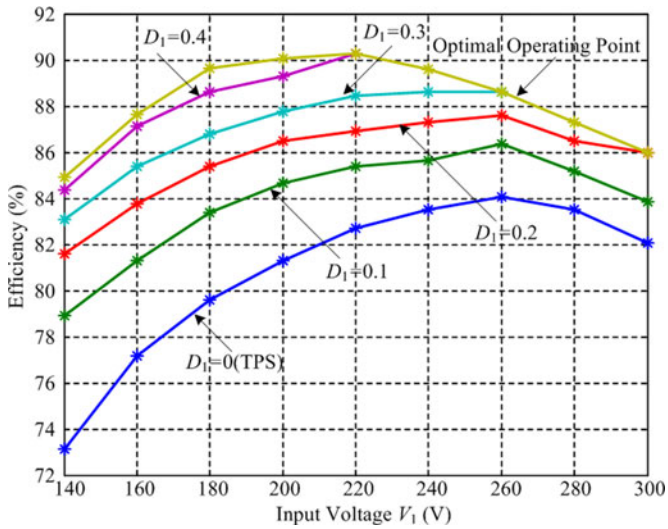


Fig. 21. Curves of the efficiency curves varied with V_1 ($k < 1$) when D_1 is specified.

VII. Conclusion

IBDC is an everlasting key component to realize power distribution between energy generation systems and storage systems in microgrids. In order to overcome the inherent disadvantages of TPS control of IBDC, a novel EPS control is proposed for power distribution in microgrid in this paper. From the theoretical analysis and the experiments, it can be found that EPS control has the following features: 1) EPS control expands regulating range of transmission power and enhances regulating flexibility. 2) EPS control reduces power-circulating flow, and thus reduces conduction losses and improves the system efficiency. 3) EPS control reduces current stress, and thus reduces switching losses and prolongs the service life of devices. For the same power level, the devices can be selected with lower stress levels, which saves the cost. 4) EPS control is simple in principle and easy to implement.

References

[1] R. H. Lasseter, "Smart distribution: Coupled microgrids," *Proc. IEEE.*, vol. 99, no. 6, pp. 1074–1082, Jun. 2011.

[2] P. Tenti, H. K. M. Paredes, and P. Mattavelli, "Conservative power theory, a framework to approach control and accountability issues in smart microgrids," *IEEE Trans. Power Electron.*, vol. 26, no. 3, pp. 664–673, Mar. 2011.

[3] R. Majumder, A. Ghosh, G. Ledwich, and F. Zare, "Power management and power flow control with back-to-back converters in a utility connected microgrid," *IEEE Trans. Power System.*, vol. 25, no. 2, pp. 821–834, May 2010.

[4] A. K. Abdelsalam, A. M. Massoud, S. Ahmed, and P. N. Enjeti, "High-performance adaptive perturb and observe MPPT technique for photovoltaic-based microgrids," *IEEE Trans. Power Electron.*, vol. 26, no. 4, pp. 1010–1021, Apr. 2011.

[5] J. M. Guerrero, J. C. Vasquez, J. Matas, M. Castilla, and L. G. Vicuna, "Control strategy for flexible microgrid based on parallel line-interactive UPS system," *IEEE Trans. Ind. Electron.*, vol. 56, no. 3, pp. 726–736, Mar. 2009.

[6] J. Y. Kim, J. H. Jeon, S. K. Kim, C. Cho, J. H. Park, H.-M. Kim, and K.-Y. Nam, "Cooperative control strategy of energy storage system and microsources for stabilizing the microgrid during islanded operation," *IEEE Trans. Power Electron.*, vol. 25, no. 12, pp. 3037–3048, Dec. 2010.

[7] J.-H. Jeon, J. Y. Kim, H. M. Kim, S.-K. Kim, C. Cho, J.-M. Kim, J.-B. Ahn, and K.-Y. Nam, "Development of hardware in-the-loop simulation system for testing operation and control functions of microgrid," *IEEE Trans. Power Electron.*, vol. 25, no. 12, pp. 2919–2929, Dec. 2010.

[8] T. F. Wu, K. H. Sun, C. L. Kuo, and C. H. Chang, "Predictive current controlled 5-kW single-phase bidirectional inverter with wide inductance variation for dc-microgrid applications," *IEEE Trans. Power Electron.*, vol. 25, no. 12, pp. 3076–3084, Dec. 2010.

[9] M. G. Molina and P. E. Mercado, "Power flow stabilization and control of microgrid with wind generation by superconducting magnetic energy

Authorized licensed use limited to: Electricity Generating Authority of Thailand. Downloaded on December 01,2021 at 07:50:17 UTC from IEEE Xplore. Restrictions apply.

storage," *IEEE Trans. Power Electron.*, vol. 26, no. 3, pp. 910–922, Mar. 2011.
[10] J. M. Gueerrero, N. Berbel, J. Matas, J. L. Sosa, and L. G. vicuna, "Droop control method with virtual output impedance for parallel operation of uninterruptible power supply systems in a microgrid," in *Proc. IEEE Appl. Power Electron. Conf.*, 2007, pp. 1126–1132.
[11] W. Chen, P. Rong, and Z. Y. Lu, "Snubberless bidirectional DC–DC converter with new CLLC resonant tank featuring minimized switching loss," *IEEE Trans. Ind. Electron.*, vol. 57, no. 9, pp. 3075–3086, Sep. 2010.
[12] F. H. Khan and L. M. Tolbert, "Bi-directional power management and fault tolerant feature in a 5-kW multilevel DC–DC converter with modular architecture," *IET Power Electron.*, vol. 2, no. 5, pp. 595–604, Jul. 2009.
[13] C. M. Wang, C. H. Lin, and T. C. Yang, "High-power-factor soft-switched DC power supply system," *IEEE Trans. Power Electron.*, vol. 26, no. 2, pp. 647–654, Feb. 2011.
[14] P. Das, S. A. Mousavi, and G. Moschopoulos, "Analysis and design of a nonisolated bidirectional ZVS-PWM DC–DC converter with coupled inductors," *IEEE Trans. Power Electron.*, vol. 25, no. 10, pp. 2630–2641, Oct. 2010.
[15] S. Inoue and H. Akagi, "A bidirectional DC–DC converter for an energy storage system with galvanic isolation," *IEEE Trans. Power Electron.*, vol. 22, no. 6, pp. 2299–2306, Nov. 2007.
[16] W. H. Li, W. C. Li, Y. Deng, and X. N. He, "Single-stage single-phase high-step-up ZVT boost converter for fuel-cell microgrid system," *IEEE Trans. Power Electron.*, vol. 25, no. 12, pp. 3057–3065, Dec. 2010.
[17] Y. H. Xie, J. Sun, and S. F. James, "Power flow characterization of a bidirectional galvanically isolated high-power DC/DC converter over a wide operating range," *IEEE Trans. Power Electron.*, vol. 25, no. 1, pp. 54–65, Jan. 2010.
[18] M. Nymand and M. A. E. Andersen, "High-efficiency isolated boost DC–DC converter for high-power low-voltage fuel-cell applications," *IEEE Trans. Ind. Electron.*, vol. 57, no. 2, pp. 505–514, Feb. 2010.
[19] I. Y. Chung, W. X. Liu, K. Schoder, and D. A. Cartes, "Integration of a bi-directional DC–DC converter model into a real-time system simulation of a shipboard medium voltage DC system," *Int. J. Electr. Power Syst. Res.*, vol. 81, pp. 1051–1059, 2011.
[20] K. R. Wang, F. C. Lee, and J. Lai, "Operation principles of bi-directional full-bridge DC-DC converter with unified soft-switching scheme and soft-starting capability," in *Proc. IEEE Appl. Power Electron. Conf.*, 2000, pp. 111–118.
[21] C. Zhao, S. D. Round, and J. W. Kolar, "An isolated three-port bidirectional DC–DC converter with decoupled power flow management," *IEEE Trans. Power Electron.*, vol. 23, no. 5, pp. 2443–2453, Sep. 2008.
[22] J. Kim, H. S. Song, and K. Nam, "Asymmetric duty control of a dual-half-bridge dc/dc converter for single-phase distributed generators," *IEEE Trans. Power Electron.*, vol. 26, no. 3, pp. 973–982, Mar. 2011.
[23] G. G. Oggier, G. O. Garcia, and A. R. Oliva, "Modulation strategy to operate the dual active bridge DC–DC converter under soft switching in the whole operating range," *IEEE Trans. Power Electron.*, vol. 26, no. 4, pp. 1228–1236, Apr. 2011.
[24] B. Hua and M. Chris, "Eliminate reactive power and increase system efficiency of isolated bidirectional dual-active-bridge DC–DC converters using novel dual-phase-shift control," *IEEE Trans. Power Electron.*, vol. 23, no. 6, pp. 2905–2914, Nov. 2008.
[25] H. Fan and H. Li, "A novel phase-shift bidirectional DC–DC converter with an extended high-efficiency range for 20kVA solid state transformer," in *Proc. IEEE Energy Convers. Congr. Expo. (ECCE).*, 2010, pp. 3870–3876.



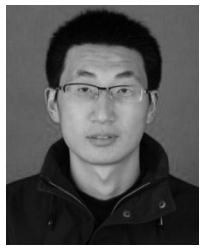
Biao Zhao (S'11) received the B.S. degree from the Department of Electrical Engineering, Dalian University of Technology, Dalian, China, in 2009. He is currently working toward the Ph.D. degree in the Department of Electrical Engineering, Tsinghua University, Beijing, China.

His current research interests include medium-voltage power conversion system, bidirectional isolated DC–DC converters, and uninterruptible power supply system.



Qingguang Yu (M'01) received the B.S. and M.S. degrees from Liaoning Engineering Technology University, Fuxin, China, in 1989 and 1991, respectively, and the Ph.D. degree from China University of Mining and Technology, Beijing, China, in 1994, all in electrical engineering.

After 2 years of Post-Doctoral research work in Electrical Engineering Department, he is currently working as an Associate Professor with the Institute of Flexible AC Transmission System (FACTS) of Tsinghua University in Beijing. His current research interests include medium-voltage power conversion system, motor drive and control, and power system automation FACTS in power plant and station.



Weixin Sun received the B.S. degree from Yanshan University, Qinghuangdao, China, in 2009, and the M.S. degree from Tsinghua University, Beijing, China, in 2011, all in electrical engineering.

He is currently working with China Power Engineering Consulting Group Corporation, North China Power Engineering Co. Ltd.

Authorized licensed use limited to: Electricity Generating Authority of Thailand. Downloaded on December 01,2021 at 07:50:17 UTC from IEEE Xplore. Restrictions apply.